

Article

Evaluation of Thermoelectric Generators under Mismatching Conditions

Daniel Sanin-Villa *, Oscar D. Monsalve-Cifuentes  and Elkin E. Henao-Bravo 

Faculty of Engineering, Department of Mechatronics and Electromechanics, Instituto Tecnológico Metropolitano, Medellín 050034, Colombia; oscarmonsalve204998@correo.itm.edu.co (O.D.M.-C.); elkinhenao@itm.edu.co (E.E.H.-B.)

* Correspondence: danielsanin@itm.edu.co

Abstract: Due to the wide usability of thermoelectric generators (TEG) in the industry and research fields, it is plausible that mismatching conditions are present on the thermal surfaces of a TEG device, which induces negative-performance effects due to uneven surface temperature distributions. For this reason, the objective of this study is to characterize numerically the open-circuit electric output voltage of a TEG device when a mismatching condition is applied to both the cold and hot sides of the selected N and P-type semiconductor material $\text{Bi}_{0.4}\text{Sb}_{1.6}\text{Te}_3$. A validated numerical simulation paired with a parametric study is conducted using the Thermal-Electric module of ANSYS 2020 R1, for which different thermal boundary and mismatching conditions are applied while considering the temperature-dependent thermoelectrical properties of the N and P-type material. The results show an inverse relationship between the open-circuit voltage and the mismatching temperature difference. When a mismatching condition is applied on the hot side of the TEG device, the temperature-dependent electrical resistance has lower values, deriving in higher voltage results (linear tendency) compared to a mismatching condition applied to the cold side (non-linear tendency).

Keywords: thermoelectric generator; TEG; mismatch; mismatching condition; numerical simulation



Citation: Sanin-Villa, D.; Monsalve-Cifuentes, O.D.; Henao-Bravo, E.E. Evaluation of Thermoelectric Generators under Mismatching Conditions. *Energies* **2021**, *14*, 8016. <https://doi.org/10.3390/en14238016>

Academic Editors: Zhi-Gang Chen and Bertrand Lenoir

Received: 31 August 2021
Accepted: 14 October 2021
Published: 1 December 2021

Publisher's Note: MDPI stays neutral with regard to jurisdictional claims in published maps and institutional affiliations.



Copyright: © 2021 by the authors. Licensee MDPI, Basel, Switzerland. This article is an open access article distributed under the terms and conditions of the Creative Commons Attribution (CC BY) license (<https://creativecommons.org/licenses/by/4.0/>).

1. Introduction

A single thermoelectric generator (TEG) is a device composed of semiconductor materials (N and P-type) connected electrically in series and thermally in parallel (More than two modules can be electrically connected either in series or parallel) that produces electric power from a temperature difference (Seebeck effect), or cooling from an electric potential source (Peltier effect) [1]. These devices are used in a wide range of applications i.e., bio-integrated wearable devices [2], pipe heat energy waste [3], automobile exhaust heat [4,5], heat exchangers [6], combustion engines [7,8], photovoltaic systems [9–11], and space exploration [12–14].

Thermoelectric devices are subject to non-uniform temperature distributions, i.e., mismatching conditions due to environmental-operating conditions. It has been reported that the performance of working thermoelectric arrangements is lower than expected under mismatched temperature conditions [15]. Tang et al. [16] found a power loss of 11% in the performance of a TEG module under mismatched temperature conditions for automobile exhaust heat recovery, while asserting that proper isolation could reduce the losses down to 2.3%. Hakim & Lim [17] compared the performance of two interconnected thermoelectric modules, one of them under temperature mismatching conditions and the other one without them. They found an electric power difference of 45.73% at a temperature difference of $\Delta T = 340.15$ K, with the non-mismatched module producing the higher power.

Experimental studies on coupled TEG-Photovoltaic (TEG-PV) systems reported negative effects of mismatching temperature conditions, hindering efficient heat transfer, and thus lowering the expected design performance [18,19].

Material-wise, Bismuth Telluride (Bi_2Te_3) is used widely for industrial applications due to cost-benefit reasons. However, the scarcity of these materials in the earth's crust [20] compelled research laboratories to find other types of usable materials for thermoelectric applications [21]. Therefore, new materials for this application e.g., half-Heusler, skutterudites, Calcium/Manganese oxides, Magnesium silicide, and tetrahedrites are currently being used for temperature difference ranges of ($300 \leq \Delta T \leq 750$) K and withstanding maximum temperatures of ($573 \leq T_{max} \leq 1073$) K [22,23].

Furthermore, numerical studies on TEG devices have been performed underlining simulation methodologies [24,25], while others allow visualization that the methodology to mathematically model the mismatching temperature conditions for both photovoltaic cells and thermoelectric devices are similar [26,27].

Wang et al. [28] proposed a mathematic model which takes into account the temperature-dependent thermoelectrical properties and effects of convection but did not consider the temperature mismatching. Montecucco et al. [15] performed an experimental study of interconnected thermoelectric devices in series and parallel considering the temperature mismatching effect over the circuital model, not directly on the thermoelectric couples but on the whole arrangement. Wee [29] developed a theoretical analysis to solve the differential equations governing the thermoelectric devices based on the assumption of the linear variation of the temperature over P-N couples, but he neglected real physical phenomena such as temperature mismatching conditions. Ju et al. [30] performed a similar investigation considering only a linear variation of the Seebeck coefficient and electrical resistivity; no mismatching conditions were considered in the analysis. Therefore, current models neglect the combined effect of physical phenomena like thermal dependence of properties and the mismatching boundary conditions.

In literature, there are no reported models to evaluate the thermal mismatching on individual thermoelectrical couples considering the thermal variation of physical properties like Seebeck coefficient, thermal conductivity, electrical resistivity, and the dimensionless figure of merit. Therefore, this paper addresses such a problem by introducing the following contributions: first, a mathematical model to evaluate the mismatching conditions even on the cold and hot side; second, a thermoelectric simulation including the effect of temperature gradient on the thermoelectrical properties; and third, the evaluation of the efficiency of thermocouples under mismatching conditions.

The objective of this study is to characterize by means of numerical simulation the open-circuit electric output available power of a TEG device when a mismatching condition is applied to both the cold and hot sides of the TEG device considering temperature-dependent properties of the N and P-type semiconductor material $\text{Bi}_{0.4}\text{Sb}_{1.6}\text{Te}_3$.

Section 2 of the paper describes the governing equations, the thermoelectrical properties, and the methodology for the simulation. Section 3 presents the results of temperature and voltage contours and trend curves. Finally, Section 4 concludes the present work highlighting the main results.

2. Materials and Methods

2.1. Governing Equations

Figure 1 shows a thermoelectric generator (TEG) device, which is composed of thermocouples of P-type (positive) and N-type (negative) materials, and copper electrodes. A set of n -th materials can be connected electrically in series, and thermally in parallel to form a thermoelectric array. If a temperature difference $\Delta T_{TEG} = T_{hot} - T_{cold}$ is applied to the TEG device, then an open-circuit voltage V_{oc} is generated due to the Seebeck effect. When an electrical load R_L is connected to both ends of the TEG device, an electric current I flows from the N to the P material. Equation (1) defines the open-circuit voltage V_{oc} produced by the TEG device. The term $\alpha = \alpha_P - \alpha_N$ is the combined Seebeck coefficient, which relates the Seebeck coefficient for both the N and P-type materials [31].

$$V_{oc} = \alpha \Delta T_{TEG} \quad (1)$$

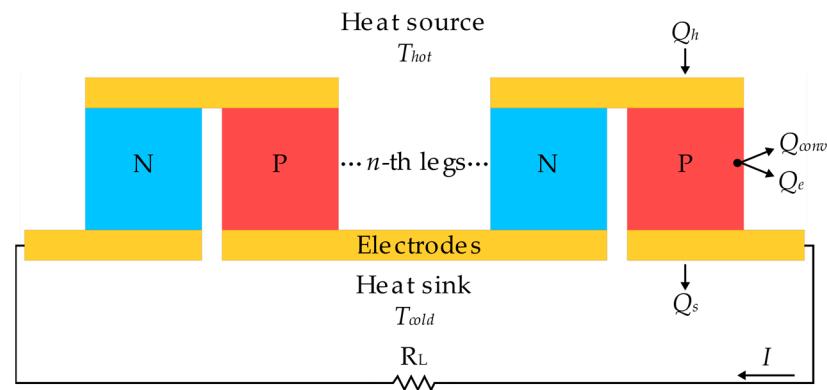


Figure 1. General configuration and energy flow of a thermoelectric generator device.

Figure 1 also shows the heat energy Q inputs and outputs present in a leg of the TEG device, whose energy balance equation must follow that $Q_h = Q_e + Q_{conv} + Q_s$, where h , e , $conv$, and s represent the heat input, heat to electrical energy conversion, heat loss due to convection, and heat energy on the heatsink, respectively. Then, the general steady-state heat flow equation is defined by (2) [32].

$$\nabla \cdot \vec{q} = \dot{q} \quad (2)$$

The left side of Equation (2) represents the divergence of the heat flux vector \vec{q} , which is defined in terms of the Fourier's law of thermal conduction $-k\nabla T$ involving the thermal conductivity k , the heat generation due to the Peltier effect $\alpha \vec{J} T$, and the electric current density vector \vec{J} , given by (3). According to [33], the electric current density can be computed as (4), where $\vec{E} = -\nabla\phi$ is the electric field intensity vector, and ρ is the electrical resistivity. In addition, the electric scalar potential ϕ is defined by (5).

$$\vec{q} = -k\nabla T + \alpha T \vec{J} \quad (3)$$

$$\vec{J} = \frac{1}{\rho} \left(\vec{E} - \alpha \nabla T \right) \quad (4)$$

$$-\nabla\phi = \rho \vec{J} + \alpha \nabla T \quad (5)$$

The right side of Equation (2) is the heat generation rate per unit volume \dot{q} , which is defined as (6).

$$\dot{q} = \rho \left| \vec{J} \right|^2 + \alpha \vec{J} \cdot \nabla T - q_{conv} \quad (6)$$

where $\rho \left| \vec{J} \right|^2$ is the Joule heating, $\alpha \vec{J} \cdot \nabla T$ is the work done against the Seebeck field, and $q_{conv} = [hP(T - T_0)]/A$ is the heat loss on the side of the TEG's legs due to convection, where the term h [W/m²K] is the heat transfer coefficient, T_0 the ambient temperature, P and A are the perimeter and area of the TEG's leg cross-section, respectively [28]. The divergence of Equation (3) using the product rule yields (7).

$$\nabla \cdot \vec{q} = -\nabla \cdot (k\nabla T) + \alpha T \left(\nabla \cdot \vec{J} \right) + \alpha \vec{J} \cdot \nabla T + T \vec{J} \cdot \nabla \alpha \quad (7)$$

For a steady-state analysis, the divergence of the electric current density vector is $\nabla \cdot \vec{J} = 0$, which ensures the continuity of the current density [34]. Furthermore, if the Seebeck coefficient is a function of temperature $\alpha(T)$, then the Thomson coefficient is defined as $\beta = T(\partial\alpha/\partial T)$ [35]. Hence, substituting Equations (6) and (7) into (2), and

accounting for the temperature dependency of the properties of the materials, Equation (2) can be rewritten for a three-dimensional case as a second-order partial differential equation with variable coefficients as (8).

$$k(T)\nabla^2 T - \beta(T)\vec{J} \cdot \nabla T + \rho(T)\left|\vec{J}\right|^2 - \frac{P}{A}h(T - T_o) = 0 \quad (8)$$

The voltage distribution throughout a control volume of a TEG device considering the electric current density vector $\nabla \cdot \vec{J} = 0$ for a steady-state condition, can be derived using Equation (5) resulting in (9), [34].

$$\nabla \cdot [\sigma(T)\nabla V] + \nabla \cdot [\sigma(T)\alpha(T)\nabla T] = 0 \quad (9)$$

where $\sigma(T) = 1/\rho$ is the electrical conductivity as a function of temperature T . The first and second terms of Equation (9) represent the electric conduction, and the distortion on the electric field caused by the thermoelectric effect, respectively [34]. Therefore, Equations (8) and (9) describe the existing thermoelectric phenomena in a TEG device.

The TEG electrical output available power P_e can be approximated using the open-circuit voltage and the temperature-dependent total internal electrical resistance $R_{total}(T)$, as Equation (10) shows, [36].

$$P_e = \frac{V_{oc}^2}{4R_{total}(T)} \quad (10)$$

The maximum efficiency of a thermoelectric material, either when the TEG device is generating electrical power or cooling, can be determined using the factor of merit Z , defined by (11), with $\alpha_P, \alpha_N; k_P, k_N; \rho_P, \rho_N$ being the Seebeck coefficients, the thermal conductivities, and the electrical resistivities of the P and N materials, respectively [37]. If Z is multiplied by the average temperature $T = (T_h - T_c)/2$, then the dimensionless figure of merit ZT is obtained, given by (12), [38].

$$Z = \frac{(\alpha_P - \alpha_N)^2}{\left[(k_P\rho_P)^{1/2} + (k_N\rho_N)^{1/2}\right]^2} \quad (11)$$

$$ZT = \frac{\alpha^2 T}{\rho k} \quad (12)$$

The efficiency of the thermoelectric generator device can be determined by relating the heat transfer rate on the hot side \dot{Q}_h and the electric output power generated P_e by the TEG device (13). The efficiency expression can be written in terms of the temperature difference $\Delta T = T_h - T_c$, the dimensionless figure of merit ZT , and the cold and hot temperatures T_c, T_h , respectively [37].

$$\eta_{TEG} = \frac{P_e}{\dot{Q}_h} = \frac{\Delta T}{T_h} \frac{\sqrt{1 + ZT} - 1}{\sqrt{1 + ZT} + \frac{T_c}{T_h}} \quad (13)$$

2.2. Thermoelectric Properties of Materials

For this article, a total of five materials constituted the studied thermoelectric module: copper, solder ($\text{Sn}_{96.5}\text{AgCu}_{0.5}$), filler (silicone elastomer), thermal interface layer (TIL), and the N and P-type material ($\text{Bi}_{0.4}\text{Sb}_{1.6}\text{Te}_3$). On the one hand, Table 1 shows the isotropic properties of thermal conductivity k , the Seebeck coefficient α , and the electrical resistivity ρ of the temperature-independent materials, except for ρ of the copper.

Table 1. Thermoelectric properties of the material used for the numerical simulation.

Material	k (W/mK)	α ($\mu\text{V/K}$)	ρ (Ωm)
Copper	400 [34]	1.80 [39]	Variable, see Figure 2
Solder ($\text{Sn}_{96.5}\text{AgCu}_{0.5}$)	64 [40]	—	1.25×10^{-7} [41]
Filler (silicone elastomer)	0.27 [42]	—	—
Thermal interface layer (TIL)	4 [43]	—	—

k : thermal conductivity; α : Seebeck coefficient; ρ : electrical resistivity.

Figure 2 shows the copper electrical resistivity ρ as a function of the temperature T , which is defined in the range of ($273.15 \leq T \leq 373.15$) K. However, for the present numerical simulation purposes, the copper ρ can be extrapolated for higher values of T .

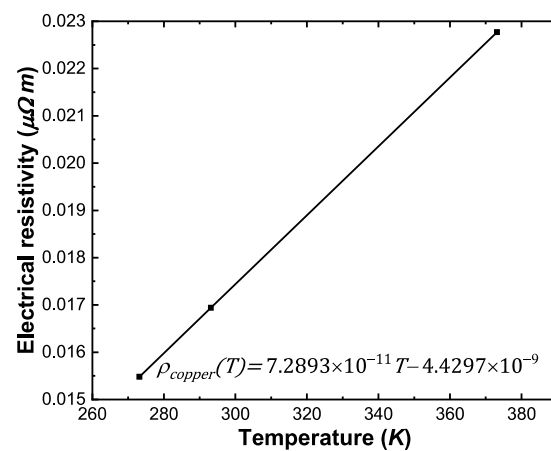


Figure 2. Copper electrical resistivity ρ as a function of temperature T for a range of ($273.15 \leq T \leq 373.15$) K [44].

On the other hand, Figure 3a shows the thermoelectrical isotropic temperature-dependent properties of the N and P-type material as the thermal conductivity k , the Seebeck coefficient α , and the electrical resistivity ρ . A range of temperature of ($300 \leq T \leq 500$) K was selected based on the experimental study of Chen et al. [45] on the $\text{Bi}_{0.4}\text{Sb}_{1.6}\text{Te}_3$ material. Figure 3b shows the dimensionless figure of merit ZT calculated using Equation (12), which reached a maximum value of $ZT = 1.52$ at $T = 350$ K.

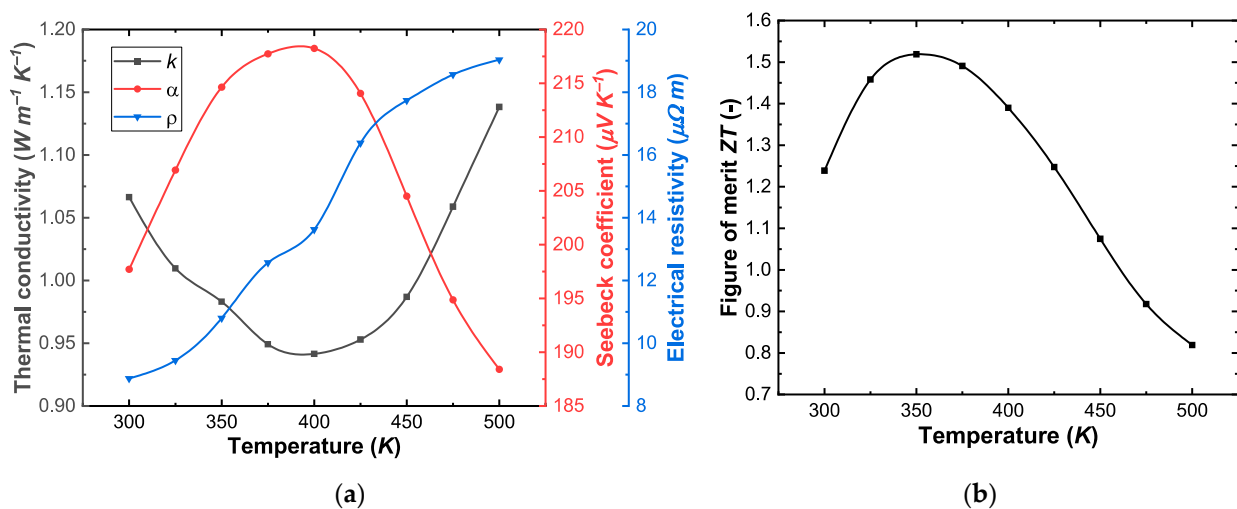


Figure 3. Thermoelectric isotropic properties of the N and P-type material $\text{Bi}_{0.4}\text{Sb}_{1.6}\text{Te}_3$: (a) Thermal conductivity k , Seebeck coefficient α , and electrical resistivity ρ as a function of temperature T ; (b) Dimensionless figure of merit ZT [45].

Table 2 shows the polynomial regressions of the isotropic thermoelectric temperature-dependent properties of the N and P-type material $\text{Bi}_{0.4}\text{Sb}_{1.6}\text{Te}_3$ and the performance ZT , where the coefficient of determination R^2 (COD), and the temperature range of the properties is specified.

Table 2. Polynomial regressions of the temperature-dependent thermoelectrical properties of the N and P-type $\text{Bi}_{0.4}\text{Sb}_{1.6}\text{Te}_3$ material for a temperature range of ($300 \leq T \leq 500$) K.

Thermoelectric Properties of $\text{Bi}_{0.4}\text{Sb}_{1.6}\text{Te}_3$	Polynomial Regressions
$k(T)$: Thermal conductivity	$1.4919 + 0.0022T - 2.1333 \times 10^{-5}T^2 + 3.1168 \times 10^{-8}T^3, R^2 = 0.9952$
$\alpha(T)$: Seebeck coefficient	$-546.7325 + 4.9569T - 0.0102T^2 + 6.4221 \times 10^{-6}T^3, R^2 = 0.9821$
$\rho(T)$: Electrical resistivity	$138.8930 - 1.0964T + 0.0029T^2 - 2.4851 \times 10^{-6}T^3, R^2 = 0.9956$
$ZT(T)$: Dimensionless figure of merit	$-22.5035 + 0.1753T - 4.1546 \times 10^{-4}T^2 + 3.1614 \times 10^{-7}T^3, R^2 = 0.9996$

According to Mackey et al. [46,47] the largest contributing sources of uncertainty on thermoelectric properties are electrical resistivity that includes the thermocouple tip radius, sample uniformity, and probe separation length. They estimated that typical samples measured with the ZEM-3 equipment, similar to ZEM-2 used by Chen et al. [45] to report the thermoelectrical properties presented in Figure 3, was about $\pm 7.0\%$ across any measurement of temperature.

2.3. Validation Study of the Numerical Model

2.3.1. TEG Device Three-Dimensional Model and Mesh

Figure 4 shows an isometric view of the studied TEG device and the general dimensions. The model is composed of one pair of P-type material (red), and one pair of N-type material (dark blue), 5 copper electrodes (orange), which is composed of 3 large and 2 small-size copper electrodes. A filler (light blue), and the thermal interface layer TIL (purple). The 3D model was meshed using the module Mesh of ANSYS 2020 R1. Additionally, Figure 5a presents the mesh independence study of the model, in which 7 iterations were executed, and the open-circuit voltage was considered as the parameter of interest. A mesh with 32,832 elements with 141,375 nodes and a maximum mesh element size of 1×10^{-4} m was selected due to the percentage error of 0.06% compared to the next iteration. Figure 5b presents a three-dimensional view of the hexahedral selected mesh used for the numerical simulation.

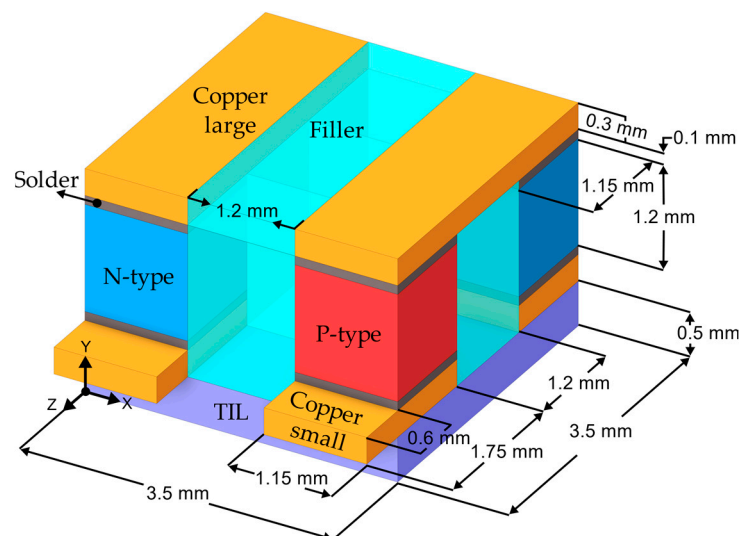


Figure 4. Isometric view of the TEG device and general dimensions of the three-dimensional model.

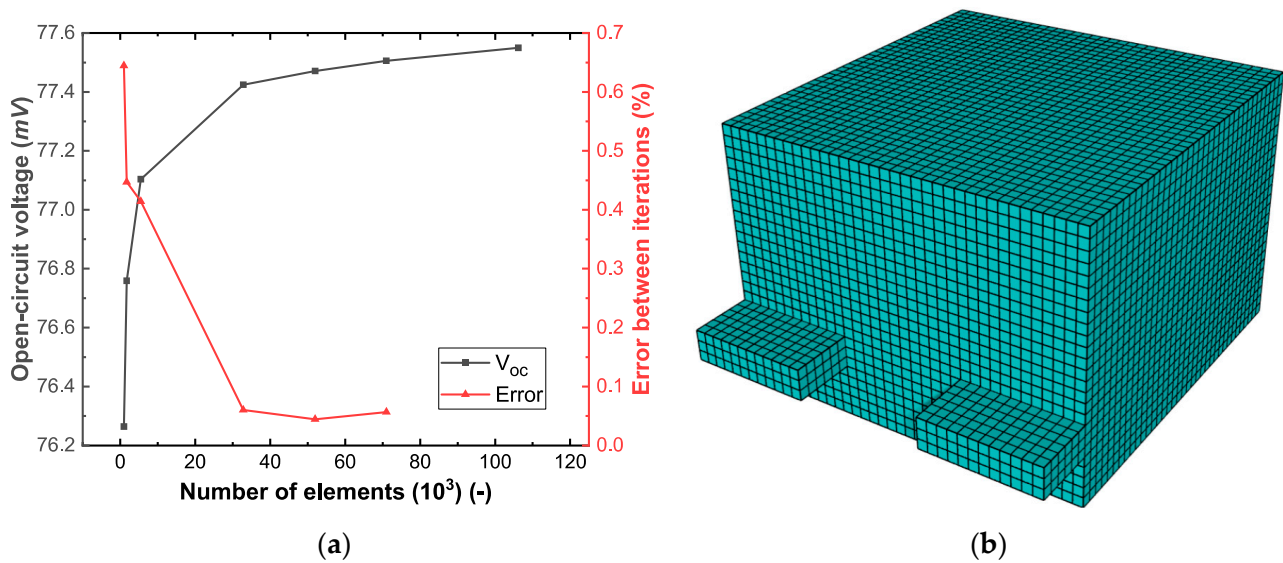


Figure 5. (a) Mesh independence study relating the open-circuit voltage, the mesh number of elements, and the relative error between iteration points; (b) Three-dimensional view of the hexahedral-based mesh.

Table 3 shows the quality parameters of the mesh that are relevant for the aggressive mechanical criterion of the APDL Mechanical solver of ANSYS such as the element quality and the Jacobian ratio (corner nodes), which limit values of 0 and 1 are bad and good quality, respectively [48,49]. The minimum and maximum values of the quality parameters are given, as well as the standard deviation and the error limit for the 3-D problem.

Table 3. Hexahedral mesh quality parameters for the aggressive mechanical criterion of Mechanical APDL of ANSYS.

Mesh Quality Parameters	Minimum Value [–]	Maximum Value [–]	Average Value [–]	Standard Deviation [–]	Error Limit Threshold [–]
Element quality	0.9512	1	0.9981	3.9829×10^{-3}	$< 5 \times 10^{-4}$
Jacobian ratio (corner nodes)	0.8568	1	0.9965	8.6903×10^{-3}	< 0.025

2.3.2. Comparison between Experimental Data and Numerical Model Results

Validation of the simulation was performed comparing the numerical open-circuit voltage V_{OC} of the TEG device model used in the simulation with the experimental open-circuit voltage of the commercial thermoelectric generator module GM250-449-10-12 of the manufacturer (European Thermodynamics Ltd., Kibworth, UK) [50]. The boundary temperatures of the hot T_h and cold T_c side of the TEG device were applied uniformly on the surface (no mismatched temperatures). The thermoelectric properties of the N- and P-type materials of the thermoelectric generator module GM250-449-10-12 used for the numerical model are reported in Figure 6.

Montecucco et al. [15] studied the same commercial thermoelectric generator (GM250-449-10-12) and reported that the module was composed of 449 thermoelectric couples/pairs of N- and P-type materials. This allowed to scale up the voltage of the numerical simulation according to the couples contained in the commercial TEG module. The comparison of the numerical and experimental open-circuit voltage V_{OC} is reported in Figure 7. A good agreement between the experimental and numerical values can be seen, confirms the validity of the numerical model used in the manuscript.

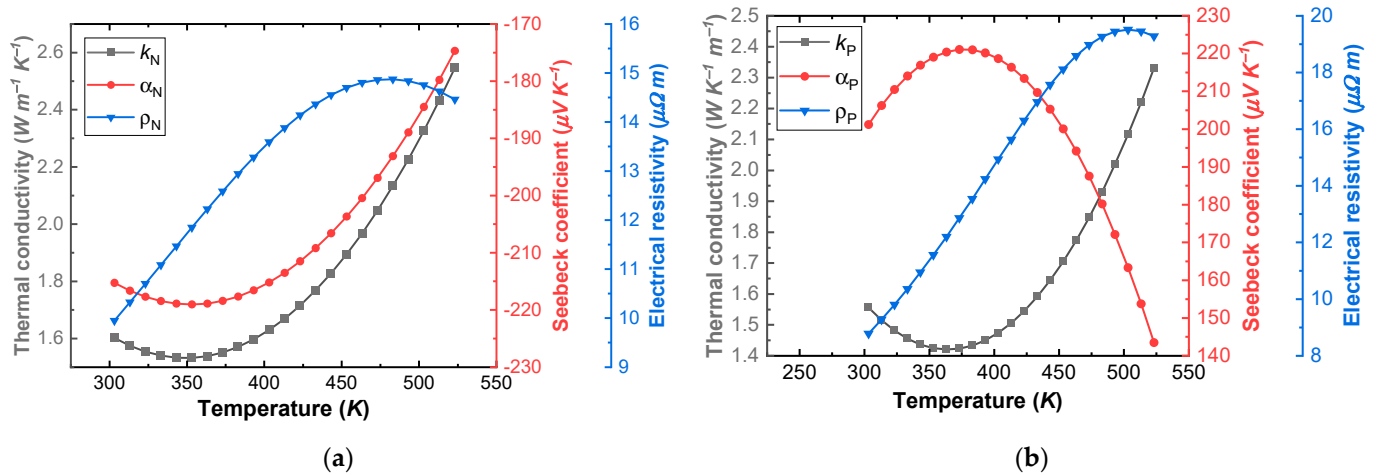


Figure 6. Thermoelectrical properties of the commercial thermoelectric generator GM250-449-10-12 of the European Thermodynamics Ltd. manufacturer. (a) For the N-type material. (b) For the P-type material [50].

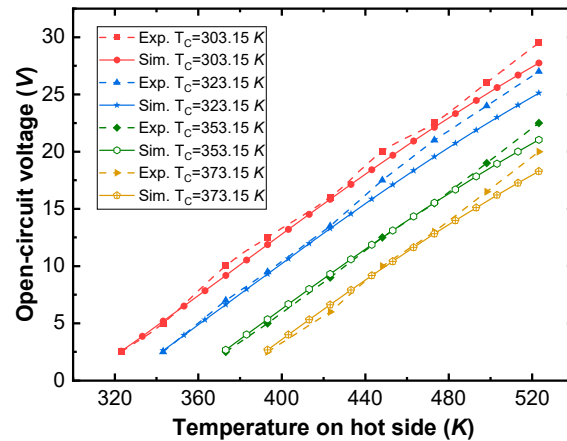


Figure 7. Validation of the numerical model comparing with the experimental open-circuit voltage of the commercial thermoelectric generator device GM250-449-10-12. The dotted lines represent the experimental (Exp.) data of the commercial TEG device obtained from [50]. The continuous lines represent the simulation (Sim.) results.

2.3.3. Verification of Numerical Thermal Efficiency

A comparison between the numerical and theoretical thermal efficiencies was carried out only for non-mismatching conditions cases, as shown in Figure 8. The theoretical values of thermal efficiency for non-mismatching conditions are calculated using Equation (13). That equation does not consider any uneven temperature distributions on both the hot and cold sides of the TEG device neither the thermoelectric variable properties.

Numerical thermal efficiency results are higher than those computed with Equation (13). A temperature-independent mean value of the dimensionless figure of merit was used ($\overline{ZT} = (T_h + T_c)/2$), where T_h and T_c represent the temperature on the hot and cold sides of the TEG device. Lastly, we consider the relative error acceptable due to the assumption of ZT to compute the theoretical thermal efficiency.

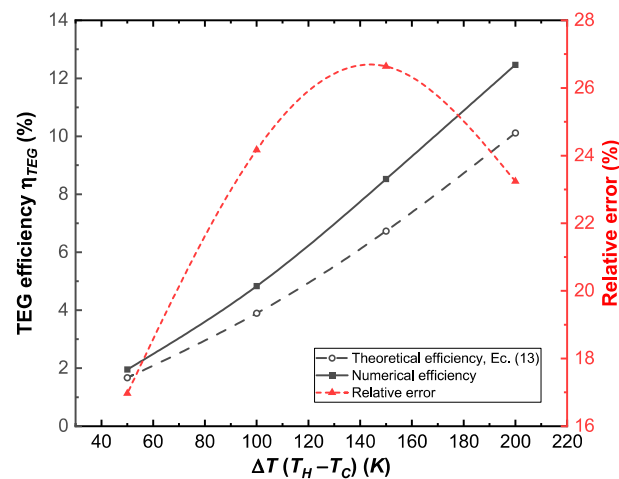


Figure 8. Theoretical and numerical comparison of the thermal efficiency of the TEG device for non-mismatching conditions. For the theoretical thermal efficiency, a constant mean value for the dimensionless figure of merit was used, defined as $\overline{ZT} = (T_h + T_c)/2$.

2.4. Boundary Conditions and Parametric Studies

The thermoelectric device shown in Figure 4 was simulated with the commercial solver code of Mechanical APDL using the Thermo-Electric module of ANSYS 2020 R1. Two simulations, which considered two cases of mismatching conditions, were executed by a 12-core Intel[®] Xeon CPU E5-2667 at 2.90 GHz, and 32 GB of RAM workstation. Both simulations assumed no heat transfer by convection $Q_{conv} = 0$ nor the effects of radiation $Q_{rad} = 0$ due to the considered low temperature gradients [51].

2.4.1. Numerical Simulation of the Mismatching Condition on the Heat Side (Bottom Surfaces) of the TEG Device

Figure 9 shows the Dirichlet thermoelectric boundary conditions for this simulation, which are assigned as follows: firstly, a thermal boundary condition T_{cold} is placed on the three upper surfaces of the model, which represent the ambient temperature or heatsink. Also, an electromagnetic boundary condition V_{ref} , which represents the reference voltage, is placed on the electrode of the P-type material, see Figure 9a. Secondly, the bottom surface has two thermal boundary conditions that represent the mismatching condition ($\Delta T_{mismatching} = T_{hot,max} - T_{hot,variable}$), where one of them is the surface temperature $T_{hot,max}$, which remain constant and is the highest temperature value; next to the previous-mentioned surface, lies the variable temperature $T_{hot,variable}$, which generates the mismatching temperature gradient on the bottom surface of the TEG device, see Figure 9b. An example of the definition of the thermoelectric boundary conditions, e.g., the temperature on the cold side T_{cold} , the voltage reference V_{ref} , and the temperatures of the hot side $T_{hot,max}$ and $T_{hot,variable}$, is given in Figure 9 representing the first row of the parametric conditions described in Table 4.

Table 4. Parametric study values of the thermoelectric boundary conditions of the mismatching condition on the heat side (bottom surfaces) of the TEG module.

$T_{hot,max}$ [K]	$T_{hot,variable}$ [K]	T_{cold} [K]	V_{ref} [V]
500	$(300 \leq T_{hot,variable} \leq 500)$, steps of 10 K	300	0
	$(350 \leq T_{hot,variable} \leq 500)$, steps of 10 K	350	
	$(400 \leq T_{hot,variable} \leq 500)$, steps of 10 K	400	
	$(450 \leq T_{hot,variable} \leq 500)$, steps of 10 K	450	

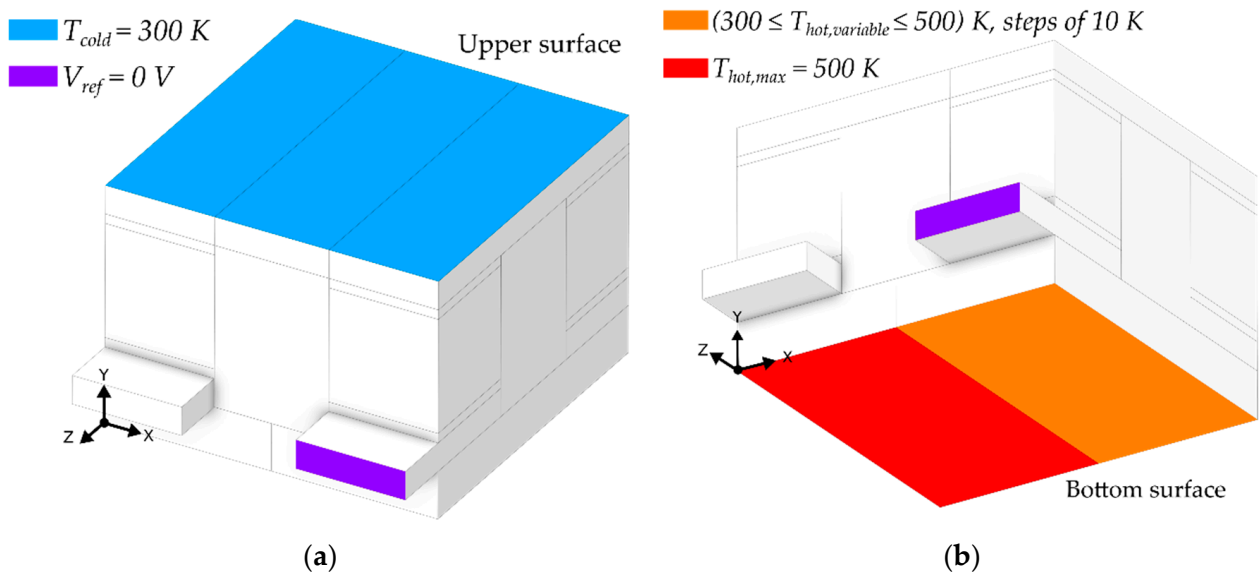


Figure 9. Dirichlet thermoelectric boundary conditions for the mismatching condition simulation on the heat side surfaces (bottom surface). (a) Thermal boundary condition temperature T_{cold} (ambient, upper surface), and electromagnetic voltage reference V_{ref} (ground) boundary conditions; (b) Thermal boundary conditions $T_{hot,max}$ and on the bottom surfaces (mismatching condition on heat side).

Table 4 describes the parametric study simulation of the mismatching condition on the heat side, see Figure 9. The temperature $T_{hot,max}$ and the electromagnetic boundary condition V_{ref} remained constant throughout the simulation at a value of 500 K and 0 V, respectively. The temperature $T_{hot,variable}$ changed within a range of $300 \leq T_{hot,variable} \leq 500$ K with steps of 10 K as the ambient temperature T_{cold} increased from 300 to 450 K.

2.4.2. Numerical Simulation of the Mismatching Condition on the Heatsink (Upper Surfaces) of the TEG Device

Figure 10 shows the Dirichlet thermoelectric boundary conditions for the mismatching condition on the heatsink surfaces, which are assigned as follows: firstly, the upper surface has two thermal boundary conditions that represent the mismatching condition ($\Delta_{mismatching} = T_{cold,min} - T_{cold,variable}$), which are the surface temperature $T_{cold,min}$ and $T_{cold,variable}$ that generate the mismatching temperature gradient on the upper surface of the TEG device. Also, an electromagnetic boundary condition V_{ref} , which represents the reference voltage, is placed on the electrode of the P-type material, see Figure 10a. Secondly, a constant thermal boundary condition T_{hot} is placed on the bottom surface of the model, which represent the heat side temperature, see Figure 10b. Additionally, an example of the definition of the thermoelectric boundary conditions e.g., the temperatures of the cold side $T_{cold,variable}$ and $T_{cold,min}$, the temperature on the hot side T_{hot} , and the voltage reference V_{ref} , is given in Figure 10 representing the first row of the parametric conditions described in Table 5.

Table 5. Parametric study values of the thermoelectric boundary conditions of the mismatching condition on the heatsink (upper surfaces) of the TEG module.

T_{hot} [K]	$T_{cold,variable}$ [K]	$T_{cold,min}$ [K]	V_{ref} [V]
500	$(300 \leq T_{cold,variable} \leq 500)$, steps of 10 K	300	0
	$(350 \leq T_{cold,variable} \leq 500)$, steps of 10 K	350	
	$(400 \leq T_{cold,variable} \leq 500)$, steps of 10 K	400	
	$(450 \leq T_{cold,variable} \leq 500)$, steps of 10 K	450	

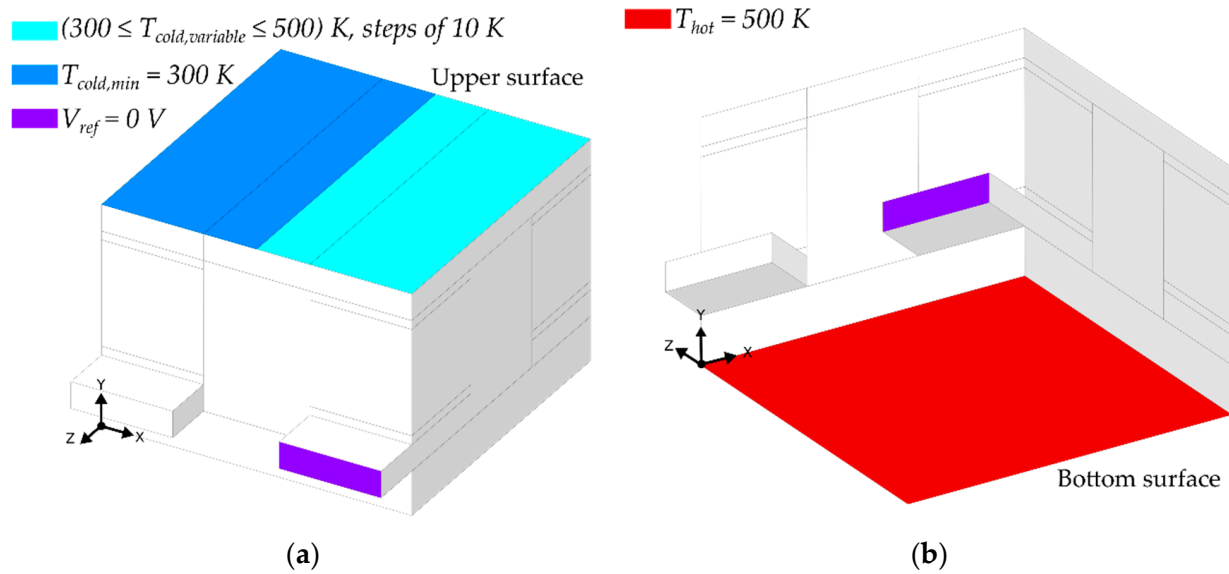


Figure 10. Dirichlet thermoelectric boundary conditions for the mismatching condition simulation on the heatsink surfaces (upper surface). (a) Thermal boundary conditions $T_{cold,min}$ and $T_{cold,variable}$ (mismatching condition on heatsink), and the voltage reference V_{ref} electromagnetic boundary condition; (b) Constant thermal boundary condition T_{hot} on the bottom surfaces.

Table 5 describes the parametric study simulation of the mismatching condition on the heatsink (upper surface), see Figure 10. The temperature T_{hot} , and the electromagnetic boundary condition V_{ref} remained constant throughout the simulation at a value of 500 K and 0 V, respectively. The temperature $T_{cold,variable}$ changed within a range of $(300 \leq T_{hot,variable} \leq 500)$ K with steps of 10 K as the temperature $T_{cold,min}$ increased from 300 to 450 K.

3. Results and Discussion

To calculate the total internal resistance of the TEG device, the geometric properties of the temperature-dependent materials are needed. In this manner, Table 6 shows the geometric properties of the copper, which has two sizes (see Figure 4), the N and P-type materials, and the solder.

Table 6. Geometric properties of the N and P-type, copper, and solder materials. H : height; W : width; D : depth; A : area.

Material	Number of Components	W x -Coordinate [m]	H y -Coordinate [m]	D z -Coordinate [m]	A [m ²]
N and P-type	4 (2 N and 2 P)	0.00150	0.00120	0.00150	2.25×10^{-6}
Copper (large)	3	0.00150	0.00030	0.00350	5.25×10^{-6}
Copper (small)	2	0.00150	0.00030	0.00175	2.63×10^{-6}
Solder	8	0.00150	0.0001	0.00150	2.25×10^{-6}

However, the total internal resistance in every point of the thermoelectric material is hard to calculate due to the three-dimensional temperature gradients induced by the mismatching conditions on the TEG device. For this reason, the total internal resistance of the copper and the N-P-type materials of the TEG module was calculated applying the mean value theorem to the polynomial regressions of the resistivities of the copper $\rho_{copper}(T)$ and the N and P-type materials $\rho_{N-P}(T)$, see Figure 2 and Table 2 for the polynomial regressions, respectively.

On the one hand, the mean value of the resistivity of the N and P-type materials $\rho_{N-P}(T)$ for the simulation of the mismatching condition on the heat side (see Section 2.4.1) is defined by the piecewise-defined function in Equation (14).

$$\bar{\rho}_{N-P, \text{ mismatching on } T_H}(T) = \begin{cases} \rho_{N-P}(T), & \text{if } T_{hot,variable} = T_{cold} \\ \left(\frac{1}{T_{hot,variable} - T_{cold}} \int_{T_{cold}}^{T_{hot,variable}} \rho_{N-P}(T) dT \right) + \left(\frac{1}{T_{hot,max} - T_{cold}} \int_{T_{cold}}^{T_{hot,max}} \rho_{N-P}(T) dT \right), & \text{if } T_{hot,variable} \neq T_{cold} \end{cases} \quad (14)$$

On the other hand, the mean value of the resistivity of the N and P-type materials $\rho_{N-P}(T)$ for the simulation of the mismatching condition on the cold side (see Section 2.4.2) is defined by the piecewise-defined function in Equation (15).

$$\bar{\rho}_{N-P, \text{ mismatching on } T_C}(T) = \begin{cases} \rho_{N-P}(T), & \text{if } T_{hot} = T_{cold,variable} \\ \left(\frac{1}{T_{hot} - T_{cold,min}} \int_{T_{cold,min}}^{T_{hot}} \rho_{N-P}(T) dT \right) + \left(\frac{1}{T_{hot} - T_{cold,variable}} \int_{T_{cold,variable}}^{T_{hot}} \rho_{N-P}(T) dT \right), & \text{if } T_{hot} \neq T_{cold,variable} \end{cases} \quad (15)$$

The temperature-dependent total internal resistance $R_{total}(T)$ of the TEG device is calculated using Equation (16), where W_{N-P} , A_{N-P} , and $\rho_{N-P}(T)$ are the width, area, and the variable resistivity of the N and P type materials, respectively. $R_{copper,large}$, $R_{copper,small}$ and R_{solder} are the constant resistivities of the temperature-independent materials.

$$R_{total}(T) = \frac{2W_{N-P}[\rho_{N-P}(T)]}{A_{N-P}} + R_{copper,large} + R_{copper,small} + R_{solder} \quad (16)$$

Figure 11 shows the temperature-dependent total internal resistance $R_{total}(T)$ of the TEG device compared to the mismatching temperature difference $\Delta T_{mismatching}$. Figure 11a presents $R_{total}(T)$ for the mismatching condition on the heat side (bottom surfaces), in which can be observed the decreasing electrical resistance as the delta of mismatching $\Delta T_{mismatching}$ increases. This is because as $\Delta T_{mismatching}$ on the hot side is higher, the temperature on the bottom surfaces gets colder, thus decreasing the electrical resistance of the N and P-type materials. Similarly, Figure 11b shows $R_{total}(T)$ for the mismatching condition on the heatsink (upper surfaces) of the TEG device, where the increment of the mismatching temperature difference $\Delta T_{mismatching}$ causes the increment of the temperature of the upper surfaces, then raising the electrical resistance of the N and P-type materials.

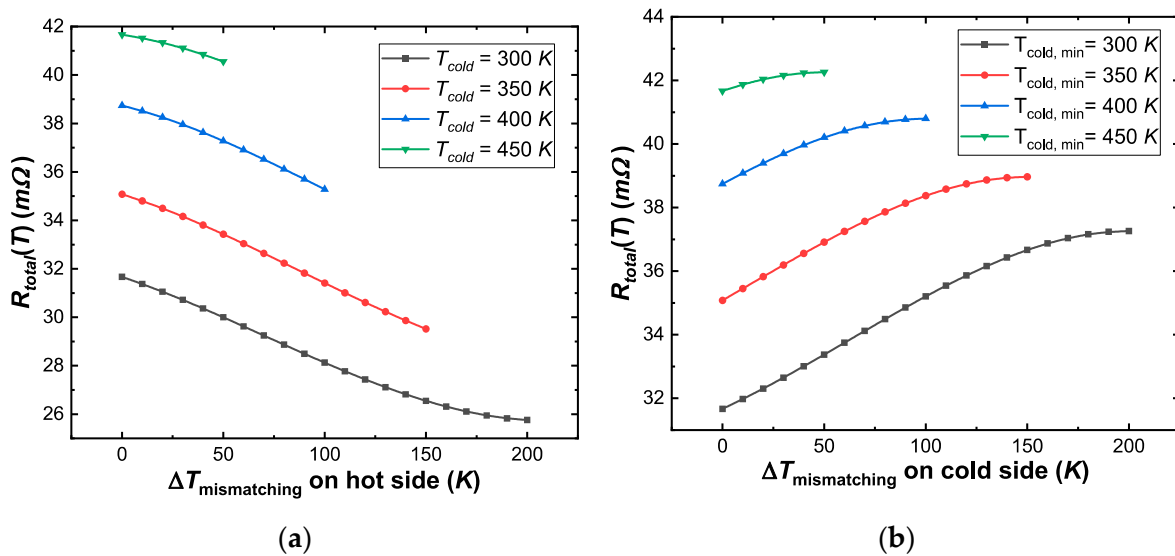


Figure 11. Temperature-dependent total internal electrical resistance $R_{total}(T)$ of the thermoelectric generator (TEG) device compared to the mismatching temperature difference $\Delta T_{mismatching}$. (a) $R_{total}(T)$ for the mismatching condition on the heat side (bottom surface). (b) $R_{total}(T)$ for the mismatching condition on the heatsink (upper surface) at a constant temperature on the heat side $T_{hot} = 500 K$.

3.1. Numerical Results and Contours of the Mismatching Condition Simulation on the Heat Side (Bottom Surface) of the TEG Device

Figure 12 presents the numerical results of the mismatching condition simulation on the heat side (bottom surfaces) of the TEG device compared to the mismatching temperature difference $\Delta T_{mismatching}$, which spans from 0 to 200 K. Figure 12a presents the open-circuit voltage V_{oc} . Figure 12b shows the electric available power P_e , calculated with Equation (10). Figure 12c shows the thermal efficiency η_{TEG} , computed as the ratio of the electric power P_e and the heat energy input Q_h , Equation (13). The above-mentioned numerical results are presented for different cold side temperatures ranging between ($300 \leq T_{cold} \leq 450$) K. Furthermore, an inverse relation can be seen between the numerical results and the increment of $\Delta T_{mismatching}$. In other words, the open-circuit voltage V_{oc} generated by the TEG device decreases because the temperature gradient between the hot and cold surfaces gets smaller as when $\Delta T_{mismatching}$ is higher. Thus, the electric power P_e and the thermal efficiency η_{TEG} also have the same behavior. Additionally, the mathematical tendency of V_{oc} and P_e is linear, whereas the tendency of η_{TEG} is exponential.

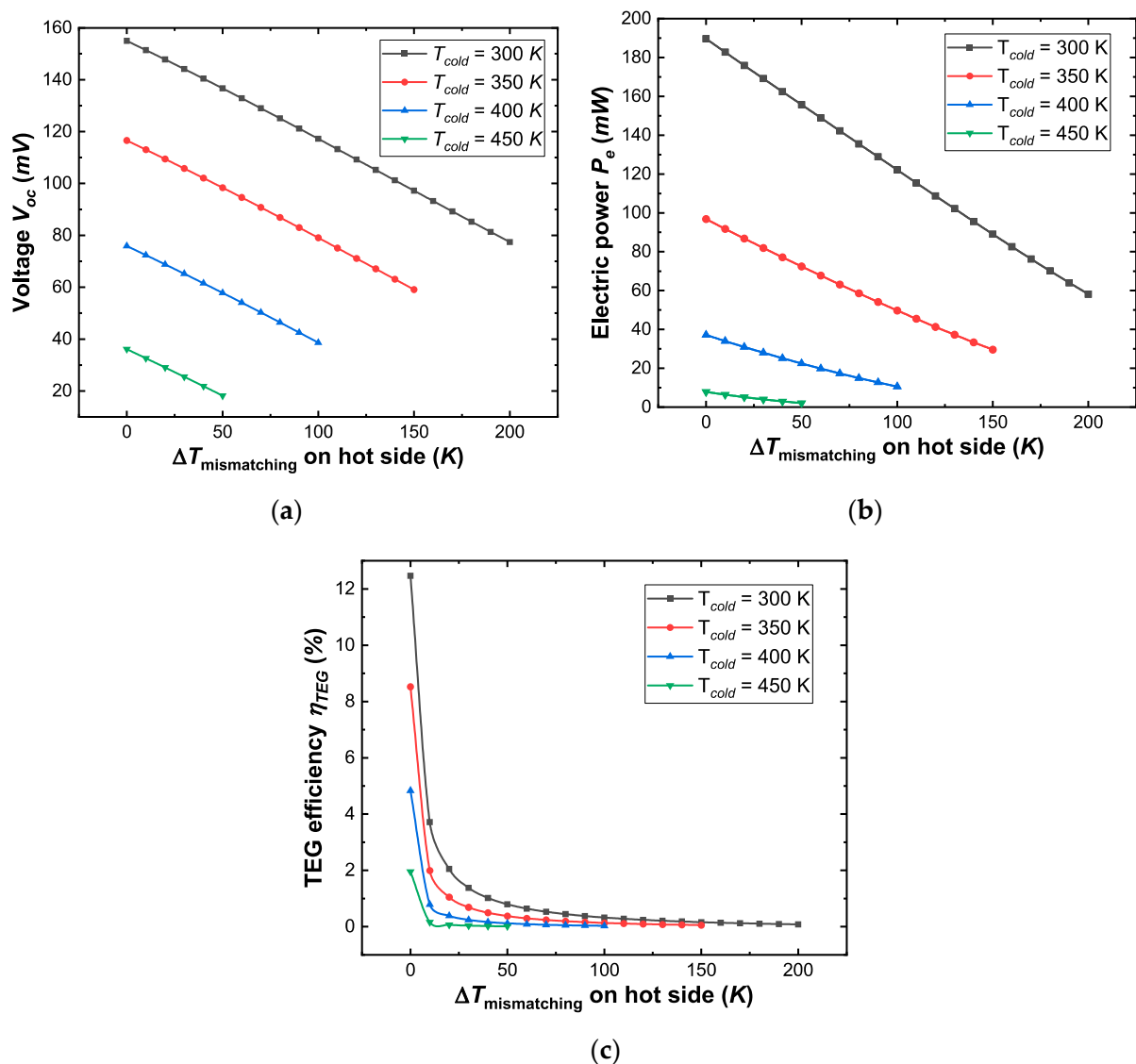


Figure 12. Numerical results of the mismatching simulation condition on the hot side (bottom surface) compared to the mismatching temperature difference $\Delta T_{mismatching}$ on the hot side of the thermoelectric generator device. (a) Open-circuit voltage V_{oc} ; (b) Electric power P_e ; (c) Thermal efficiency η_{TEG} .

Figure 13 presents the temperature and the voltage contours of the TEG device for the mismatching condition on the heat side (bottom surface) at an ambient temperature of $T_{cold} = 300$ K. On the one hand, Figure 13a–c show the two-dimensional xy -plane temperature contour distributions located at the middle of the z -coordinate of the TEG device $z = -D/2$ (D : depth) at a mismatching temperature difference $\Delta T_{mismatching} = 0, 100$ and 200 K, respectively. On the other hand, Figure 13d–f present the three-dimensional open-circuit voltage contour distributions at $\Delta T_{mismatching} = 0, 100$ and 200 K, respectively. According to the contours, the Figure 13a,d correspond the maximum electric voltage and output power production, and thus the maximum efficiency points due to the zero mismatching temperature difference $\Delta T_{mismatching} = 0$. Once a mismatching temperature difference is induced on the heat side (bottom-right surface), e.g., Figure 13b,c the open-circuit voltage V_{oc} , the electric output power P_e and the thermal efficiency η_{TEG} decrease. The above-mentioned behavior is generated by the mismatching condition on the right side of the temperature contours, which causes a reduction in the temperature gradient between the upper and bottom surfaces. The voltage not only decreases due to the reduction of the temperature gradient but also because of the Joule heating due to the flowing electric current that is generated by the left side of the TEG device, as can be seen in Figure 13e,f.

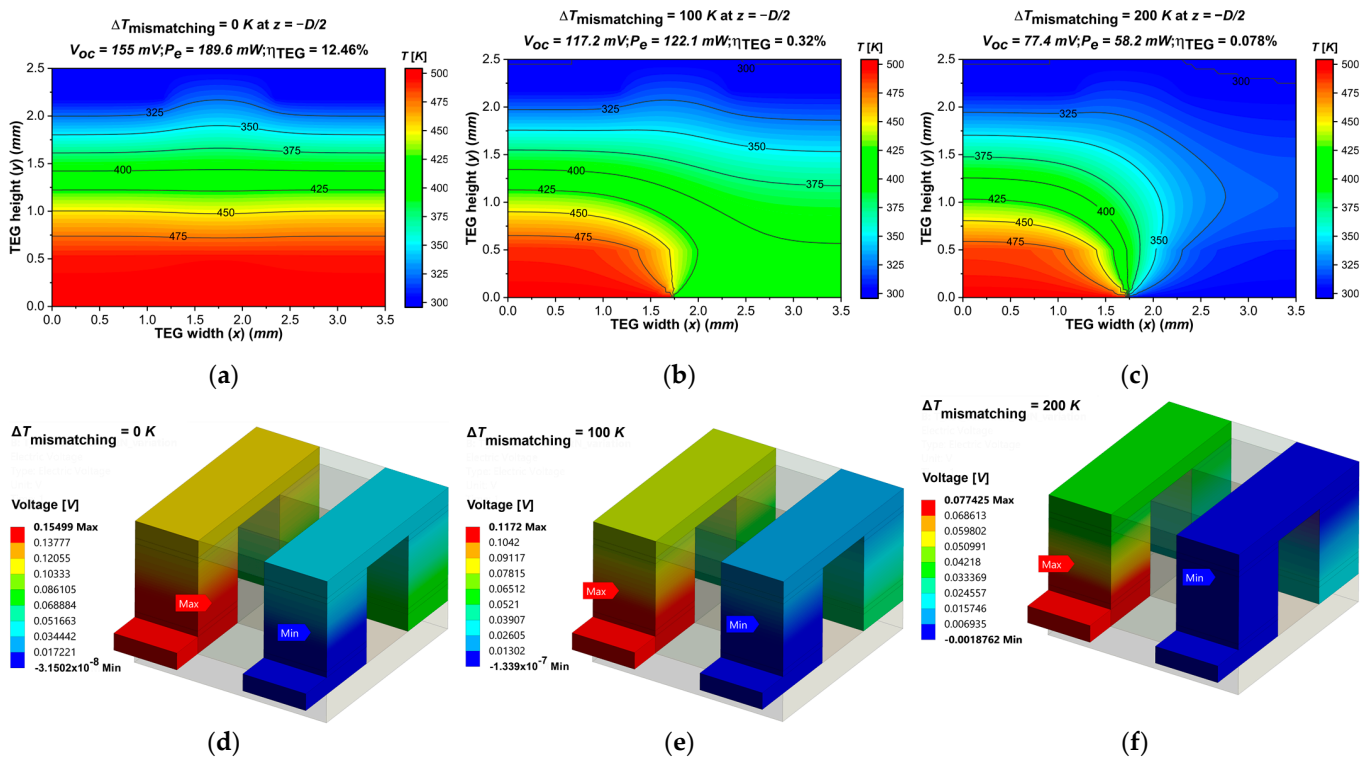


Figure 13. Contour distribution results of the mismatching condition simulation on the heat side (bottom surfaces) of the thermoelectric generator TEG device at $T_{cold} = 300$ K. (a–c) are the two-dimensional xy -plane temperature contour distributions located at the middle of the z -coordinate of the TEG device $z = -D/2$ at a mismatching temperature difference $\Delta T_{mismatching} = 0, 100$ and 200 K, respectively; (d–f) are the three-dimensional open-circuit voltage contour distributions at $\Delta T_{mismatching} = 0, 100$ and 200 K, respectively.

3.2. Numerical Results and Contours of the Mismatching Condition Simulation on the Heatsink (Upper Surface) of the TEG Device

Figure 14 presents the numerical results of the mismatching condition simulation on the cold side (upper surfaces) of the TEG device compared to the mismatching temperature difference $\Delta T_{mismatching}$, which spans from 0 to 200 K. Figure 14a presents the open-circuit voltage V_{oc} . Figure 14b shows the electric output available power P_e , calculated with Equation (10). Figure 14c shows the thermal efficiency η_{TEG} , computed as the ratio of

the electric power P_e and the heat energy input Q_h , Equation (13). These numerical results are presented for different cold-side mismatching temperatures ranging between ($300 \leq T_{cold,min} \leq 450$) K. The curve tendencies of the numerical results are inversely proportional to the increment of the mismatching temperature difference $\Delta T_{mismatching}$ due to the shortening of the temperature gradient between the upper and bottom surfaces, as the temperature boundary conditions $T_{cold,min}$ and $T_{cold,variable}$ increase. Unlike the linear tendency of V_{oc} , the electric output power P_e and the thermal efficiency η_{TEG} present a non-linear tendency.

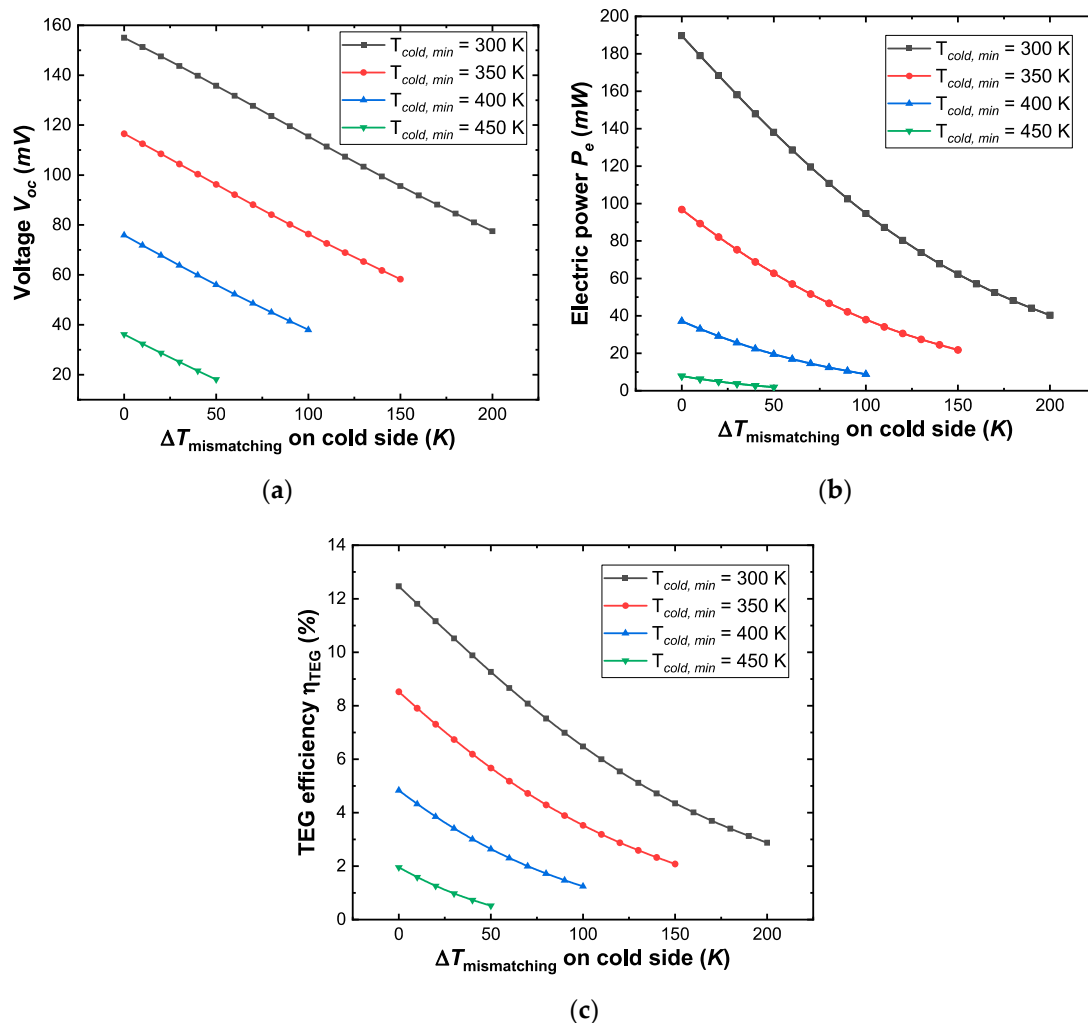


Figure 14. Numerical results of the mismatching simulation condition on the heatsink (upper surface) compared to the mismatching temperature difference $\Delta T_{mismatching}$ on the cold side of the TEG device. (a) Open-circuit voltage V_{oc} ; (b) Electric power P_e ; (c) Thermal efficiency of the TEG device η_{TEG} .

Figure 15 presents the temperature and the voltage contours of the TEG device for the mismatching condition on the heat side (bottom surface) at a mismatching temperature $T_{cold,min} = 300$ K. Figure 15a–c show the two-dimensional xy -plane temperature contour distributions located at the middle of the z -coordinate of the TEG device $z = -D/2$ (D : depth) at a mismatching temperature difference $\Delta T_{mismatching} = 0, 100$ and 200 K, respectively. On the other hand, Figure 15d–f present the three-dimensional open-circuit voltage contour distributions at $\Delta T_{mismatching} = 0, 100$ and 200 K, respectively. The Figure 15a,d correspond the maximum electric voltage and output power production, having the maximum efficiency point due to the zero mismatching temperature difference $\Delta T_{mismatching} = 0$. If a mismatching temperature difference is induced on the cold side

(upper-right surface), e.g., Figure 15b,c, the open-circuit voltage V_{oc} , the electric output power P_e and the thermal efficiency η_{TEG} decrease. The previous-mentioned behavior is generated by the mismatching condition on the upper-right side of the temperature contours, which causes a reduction in the temperature gradient between the upper and bottom surfaces of the TEG device. Also, the voltage not only decreases due to the reduction of the temperature gradient but also because of the Joule heating when the flowing electric current that is generated by the left side of the TEG device is dissipated as heat by the right side of the TEG device, as can be seen in Figure 15e,f.

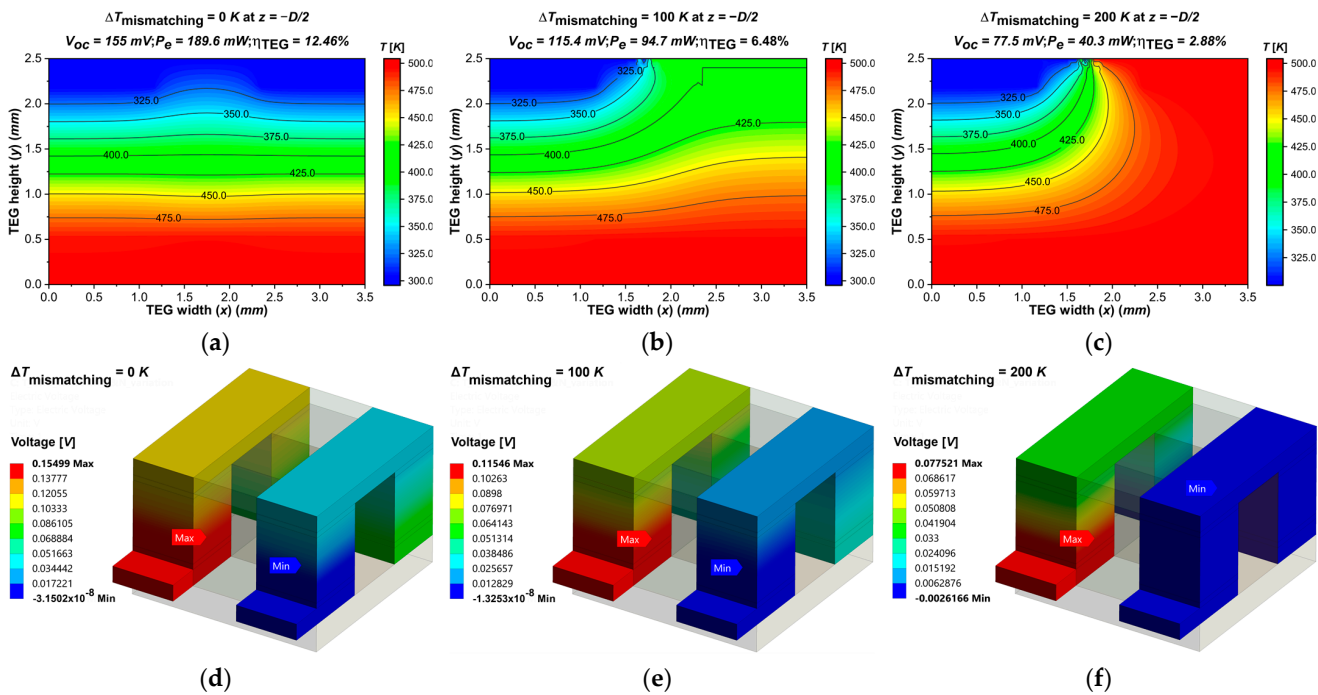


Figure 15. Contour distribution results of the mismatching condition simulation on the cold side (upper surfaces) of the thermoelectric generator TEG device at $T_{cold,min} = 300$ K. (a–c) are the two-dimensional xy -plane temperature contour distributions located at the middle of the z -coordinate of the TEG device $z = -D/2$ at a mismatching temperature difference $\Delta T_{mismatching} = 0, 100$ and 200 K, respectively; (d–f) are the three-dimensional open-circuit voltage contour distributions at $\Delta T_{mismatching} = 0, 100$ and 200 K, respectively.

3.3. Comparison of the Numerical and Contour Results between the Mismatching Conditions on the Heat and Cold Sides of the TEG Device Simulations

Figure 16 presents a comparison of the available electric power outputs P_e for the mismatching condition on the heat side (black-color curves), and cold side (red-color curves). Figure 16a presents the variation of P_e for a range of the mismatching temperature difference of ($0 \leq \Delta T_{mismatching} \leq 200$) K. Figure 16b for a range of ($0 \leq \Delta T_{mismatching} \leq 150$). Figure 16c for a range of ($0 \leq \Delta T_{mismatching} \leq 100$). Figure 16d for a range of ($0 \leq \Delta T_{mismatching} \leq 50$). From the figures it can be seen that P_e decreases linearly for the mismatching condition on the hot side T_{hot} , while P_e decreases in a non-linear way for the mismatching condition on the cold side T_{cold} . Thus, the tendency of the presented curves suggests that the mismatching condition on the cold side T_{cold} (curves in red color) of a TEG device causes the electric output power to decrease more rapidly than a mismatching condition applied on the heat side T_{hot} .

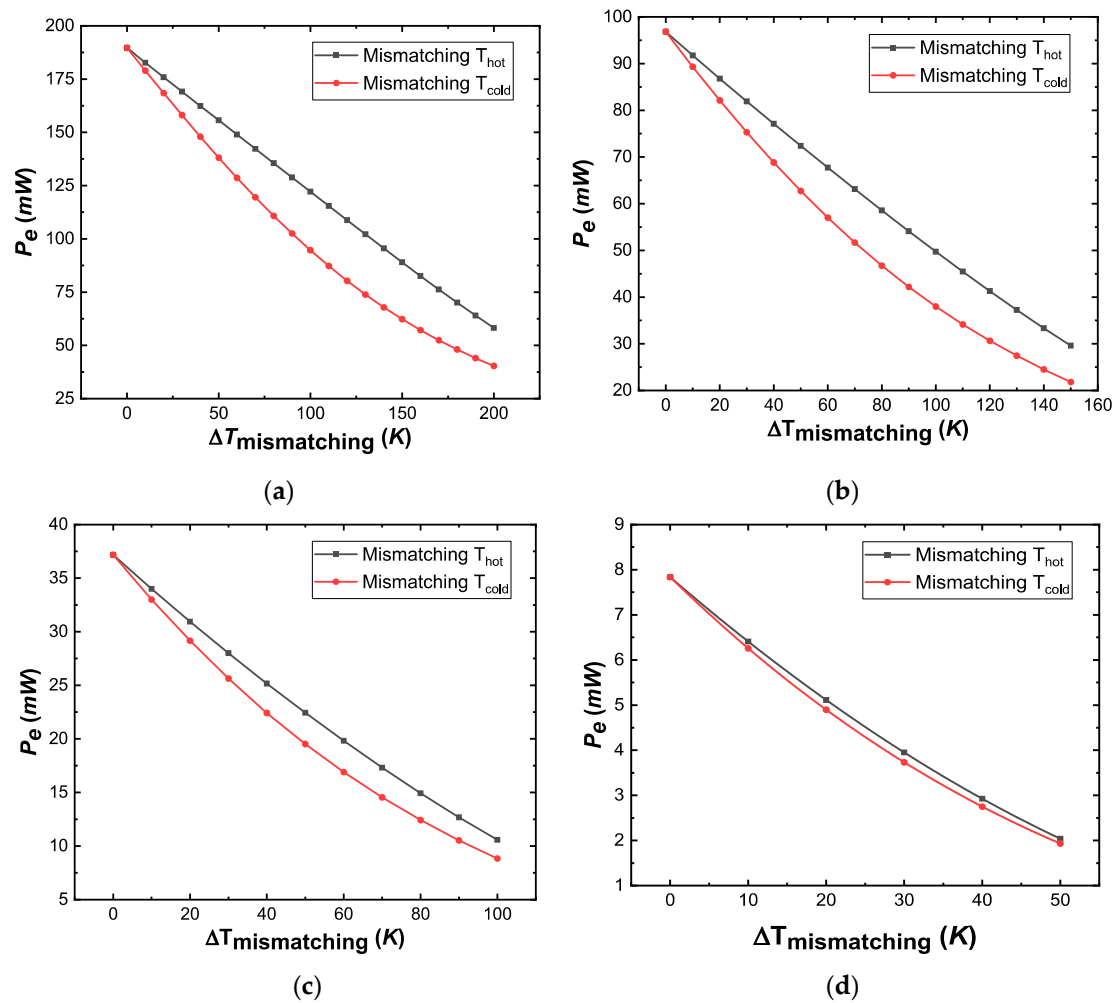


Figure 16. Comparison between the numerical electric output power P_e results and the mismatching temperature difference $\Delta T_{mismatching}$ of the mismatching condition simulations on the heat (red-color curves), and cold (black-color curves). (a) For ($0 \leq \Delta T_{mismatching} \leq 200$) K. (b) For ($0 \leq \Delta T_{mismatching} \leq 150$) K. (c) For ($0 \leq \Delta T_{mismatching} \leq 100$) K. (d) For ($0 \leq \Delta T_{mismatching} \leq 50$) K.

4. Conclusions

The generation of electric power decreases when the mismatching temperature difference increases because of the reduction of the temperature gradient between the hot and cold sides of the thermoelectric generator device (TEG). Although the values of the open-circuit voltage are similar for the mismatching conditions applied to both the cold and hot sides of the TEG, the generation of electric power is higher for a mismatching condition on the hot side than on the cold side due to the lower values of the temperature-dependent electrical resistance of the N and P-type materials when a mismatching condition is applied to the hot side. Additionally, the electric output power generated by the TEG device decreases when the mismatching temperature difference increases. Then, if a mismatching condition is applied to the hot side, the electric power decreases linearly and thus slower than that of a mismatching condition applied to the cold side, which decreases faster in a non-linear way.

In summary, there are three main contributions of this paper. The first one is the validated proposed model to evaluate thermoelectric couples under mismatching conditions. The second contribution is the inclusion of the behavior of thermoelectric properties as temperature functions. The last contribution is the evaluation of the thermal efficiency over TEG couples considering the mismatching conditions and thermal variable properties.

Author Contributions: Conceptualization, D.S.-V.; methodology, D.S.-V.; software, O.D.M.-C. and D.S.-V.; validation, O.D.M.-C. and D.S.-V.; formal analysis, D.S.-V.; investigation, D.S.-V. and O.D.M.-C.; resources, E.E.H.-B.; data curation, E.E.H.-B.; writing—original draft preparation, O.D.M.-C.; writing—review and editing, D.S.-V.; visualization, O.D.M.-C.; supervision, D.S.-V.; project administration, E.H.-B.; funding acquisition, E.E.H.-B. All authors have read and agreed to the published version of the manuscript.

Funding: This research was supported by Instituto Tecnológico Metropolitano for the Open Access fee payment under the project P21101 “Fortalecimiento Y Consolidación Del Grupo Automática, Electrónica Y Ciencias Computacionales Para Responder A Las Necesidades De Las Industrias 4.0”.

Institutional Review Board Statement: Not applicable.

Informed Consent Statement: Not applicable.

Data Availability Statement: Not applicable.

Acknowledgments: The authors thank the Instituto Tecnológico Metropolitano for the Open Access fee payment under the project P21101 “Fortalecimiento Y Consolidación Del Grupo Automática, Electrónica Y Ciencias Computacionales Para Responder A Las Necesidades De Las Industrias 4.0”.

Conflicts of Interest: The authors declare no conflict of interest.

Nomenclature

Roman letters		T_{hot}/T_H	Hot temperature (K)
A	Area (m^2)	T_{cold}/T_C	Cold temperature (K)
D	Thermoelectric device depth (m)	$T_{mismatching}$	Mismatching temperature (K)
\vec{E}	Electric field intensity vector ($V\ m^{-1}$)	TEG	Thermoelectric generator
H	Thermoelectric device height (m)	V_{oc}	Open-circuit voltage (V)
h	Heat transfer coefficient ($Wm^{-2}K^{-1}$)	W	Thermoelectric device width (m)
I	Electrical current (A)	ZT	Dimensionless figure of merit (–)
\vec{J}	Electric current density vector ($A\ m^{-2}$)		
k	Thermal conductivity ($Wm^{-2}K^{-1}$)	Greek letters	
P	Perimeter (m)	α	Combined Seebeck coefficient (VK^{-1})
P_e	Electrical output power (W)	α_P	P-type material Seebeck coefficient
Q_h	Heat energy input (J)	α_N	N-type material Seebeck coefficient (VK^{-1})
Q_e	Heat to electrical energy conversion (J)	β	Thomson coefficient
Q_{conv}	Heat loss due to convection (J)	Δ	Mathematical difference
Q_s	Heatsink energy (J)	η_{TEG}	Efficiency of the thermoelectric device (%)
\vec{q}	Heat flux vector ($W\ m^{-2}$)	ρ	Electrical resistivity (Ωm)
\dot{q}	Heat generation rate per unit volume ($W\ m^{-3}$)	$\bar{\rho}_{N-P}$	Mean value of the N and P resistivities (Ωm)
R_L	Load electrical resistance (Ω)	σ	Electrical conductivity ($s\ m^{-1}$)
R_{total}	TEG’s total electrical resistance (Ω)	ϕ	Electric scalar potential (V)

References

- Twaha, S.; Zhu, J.; Yan, Y.; Li, B. A Comprehensive Review of Thermoelectric Technology: Materials, Applications, Modelling and Performance Improvement. *Renew. Sustain. Energy Rev.* **2016**, *65*, 698–726. [[CrossRef](#)]
- Ray, T.R.; Choi, J.; Bandodkar, A.J.; Krishnan, S.; Gutruf, P.; Tian, L.; Ghaffari, R.; Rogers, J.A. Bio-Integrated Wearable Systems: A Comprehensive Review. *Chem. Rev.* **2019**, *119*, 5461–5533. [[CrossRef](#)]
- Machacek, Z.; Walendziuk, W.; Sotola, V.; Slanina, Z.; Petras, R.; Schneider, M.; Masny, Z.; Idzkowski, A.; Koziorek, J. An Investigation of Thermoelectric Generators Used as Energy Harvesters in a Water Consumption Meter Application. *Energies* **2021**, *14*, 3768. [[CrossRef](#)]
- Cózar, I.R.; Pujol, T.; Massaguer, E.; Massaguer, A.; Montoro, L.; González, J.R.; Comamala, M.; Ezzitouni, S. Effects of Module Spatial Distribution on the Energy Efficiency and Electrical Output of Automotive Thermoelectric Generators. *Energies* **2021**, *14*, 2232. [[CrossRef](#)]
- Albatati, F.; Attar, A. Analytical and Experimental Study of Thermoelectric Generator (Teg) System for Automotive Exhaust Waste Heat Recovery. *Energies* **2021**, *14*, 204. [[CrossRef](#)]

6. Ismail, B.I.; Ahmed, W.H. Thermoelectric Power Generation Using Waste-Heat Energy as an Alternative Green Technology. *Recent Patents Electr. Eng.* **2009**, *2*, 27–39. [CrossRef]
7. Kim, T.Y. Prediction of System-Level Energy Harvesting Characteristics of a Thermoelectric Generator Operating in a Diesel Engine Using Artificial Neural Networks. *Energies* **2021**, *14*, 2426. [CrossRef]
8. Dzulkfli, M.S.b.; Pesyridis, A.; Gohil, D. Thermoelectric Generation in Hybrid Electric Vehicles. *Energies* **2020**, *13*, 3742. [CrossRef]
9. Nagayoshi, H.; Tokumisu, K.; Kajikawa, T. Evaluation of Multi MPPT Thermoelectric Generator System. In Proceedings of the 26th International Conference on Thermoelectrics, Jeju, Korea, 3–7 June 2007; pp. 318–321. [CrossRef]
10. Cotfas, P.A.; Cotfas, D.T. Comprehensive Review of Methods and Instruments for Photovoltaic-Thermoelectric Generator Hybrid System Characterization. *Energies* **2020**, *13*, 6045. [CrossRef]
11. Lashin, A.; Al Turkestani, M.; Sabry, M. Performance of a Thermoelectric Generator Partially Illuminated with Highly Concentrated Light. *Energies* **2020**, *13*, 3627. [CrossRef]
12. Shure, L.I.; Harvey, J.S. *Survey of Electric Power Plants for Space Applications*; NASA: Philadelphia, PA, USA, 1965.
13. Radioisotope Power Systems. Available online: <https://rps.nasa.gov/> (accessed on 31 July 2021).
14. Voyager, the Interstellar Mission. Available online: <https://voyager.jpl.nasa.gov/mission/spacecraft/> (accessed on 31 July 2021).
15. Montecucco, A.; Siviter, J.; Knox, A.R. The Effect of Temperature Mismatch on Thermoelectric Generators Electrically Connected in Series and Parallel. *Appl. Energy* **2014**, *123*, 47–54. [CrossRef]
16. Tang, Z.B.; Deng, Y.D.; Su, C.Q.; Shuai, W.W.; Xie, C.J. A Research on Thermoelectric Generator's Electrical Performance under Temperature Mismatch Conditions for Automotive Waste Heat Recovery System. *Case Stud. Therm. Eng.* **2015**, *5*, 143–150. [CrossRef]
17. Hakim, A.; Lim, J.H. The Effect of Temperature Mismatch on Interconnected Thermoelectric Module for Power Generation. *AIP Conf. Proc.* **2020**, *2233*, 02009. [CrossRef]
18. Kidegho, G.; Njoka, F.; Muriithi, C.; Kinyua, R. Evaluation of Thermal Interface Materials in Mediating PV Cell Temperature Mismatch in PV-TEG Power Generation. *Energy Rep.* **2021**, *7*, 1636–1650. [CrossRef]
19. Ruzaimi, A.S.S.; Hassan, W.Z.W.; Azis, N.; Ya'acob, M.E.; Elianddy, E.; Aimrun, W. Performance Analysis of Thermoelectric Generator Implemented on Non-Uniform Heat Distribution of Photovoltaic Module. *Energy Rep.* **2021**, *7*, 2379–2387. [CrossRef]
20. Haxel, G.B.; James, B.H.; Greta, J.O. *Rare Earth Elements—Critical Resources for High Technology*; United States Department of the Interior Geological Survey: Reston, VA, USA, 2002; pp. 1–11.
21. Champier, D. Thermoelectric Generators: A Review of Applications. *Energy Convers. Manag.* **2017**, *140*, 167–181. [CrossRef]
22. Chen, S.; Ren, Z. Recent Progress of Half-Heusler for Moderate Temperature Thermoelectric Applications. *Mater. Today* **2013**, *16*, 387–395. [CrossRef]
23. Leblanc, S.; Yee, S.K.; Scullin, M.L.; Dames, C.; Goodson, K.E. Material and Manufacturing Cost Considerations for Thermoelectrics. *Renew. Sustain. Energy Rev.* **2014**, *32*, 313–327. [CrossRef]
24. Lin, C.X.; Kiflemariam, R. Numerical Simulation and Validation of Thermoelectric Generator Based Self-Cooling System with Airflow. *Energies* **2019**, *12*, 4052. [CrossRef]
25. Sanin-Villa, D.; Monsalve-Cifuentes, O.D.; Del Rio, J.S. Early Fever Detection on COVID-19 Infection Using Thermoelectric Module Generators. *Int. J. Electr. Comput. Eng.* **2021**, *11*, 3828–3837. [CrossRef]
26. Ramos-Paja, C.A.; Bastidas, J.D.; Saavedra-Montes, A.J.; Guinjoan-Gispert, F.; Goetz, M. Mathematical Model of Total Cross-Tied Photovoltaic Arrays in Mismatching Conditions. In Proceedings of the IEEE 4th Colombian Workshop on Circuits and Systems (CWCAS), Barranquilla, Colombia, 1–2 November 2012. [CrossRef]
27. Choi, T.; Kim, T.Y. Three-Zone Numerical Modeling Method for Predicting System-Level Waste Heat Recovery Performance of Thermoelectric Generator with Various Electrical Array Configurations. *Energy Convers. Manag.* **2021**, *240*, 114270. [CrossRef]
28. Wang, P.; Wang, K.F.; Wang, B.L.; Cui, Y.J. Modeling of Thermoelectric Generators with Effects of Side Surface Heat Convection and Temperature Dependence of Material Properties. *Int. J. Heat Mass Transf.* **2019**, *133*, 1145–1153. [CrossRef]
29. Wee, D. Analysis of Thermoelectric Energy Conversion Efficiency with Linear and Nonlinear Temperature Dependence in Material Properties. *Energy Convers. Manag.* **2011**, *52*, 3383–3390. [CrossRef]
30. Ju, C.; Dui, G.; Zheng, H.H.; Xin, L. Revisiting the Temperature Dependence in Material Properties and Performance of Thermoelectric Materials. *Energy* **2017**, *124*, 249–257. [CrossRef]
31. Thielen, M.; Sigrist, L.; Magno, M.; Hierold, C.; Benini, L. Human Body Heat for Powering Wearable Devices: From Thermal Energy to Application. *Energy Convers. Manag.* **2017**, *131*, 44–54. [CrossRef]
32. Antonova, E.E.; Looman, D.C. Finite Elements for Thermoelectric Device Analysis in ANSYS. In Proceedings of the ICT 2005 24th International Conference on Thermoelectrics, Clemson, SC, USA, 19–23 June 2005; pp. 200–203. [CrossRef]
33. Chen, W.H.; Liao, C.Y.; Hung, C.I. A Numerical Study on the Performance of Miniature Thermoelectric Cooler Affected by Thomson Effect. *Appl. Energy* **2012**, *89*, 464–473. [CrossRef]
34. Oliveira, K.S.M.; Cardoso, R.P.; Hermes, C.J.L. Numerical Assessment of the Thermodynamic Performance of Thermoelectric Cells via Two-Dimensional Modelling. *Appl. Energy* **2014**, *130*, 280–288. [CrossRef]
35. Huang, M.J.; Yen, R.H.; Wang, A.B. The Influence of the Thomson Effect on the Performance of a Thermoelectric Cooler. *Int. J. Heat Mass Transf.* **2005**, *48*, 413–418. [CrossRef]
36. Strasser, M.; Aigner, R.; Franosch, M.; Wachutka, G. Miniaturized Thermoelectric Generators Based on Poly-Si and Poly-SiGe Surface Micromachining. *Sens. Actuators A Phys.* **2002**, *97–98*, 535–542. [CrossRef]

37. Abdel-Motaleb, I.M.; Syed, M.Q. Thermoelectric Devices: Principles and Future Trends. *arXiv* **2017**, arXiv:1704.07742.
38. Snyder, G.J.; Snyder, A.H. Figure of Merit ZT of a Thermoelectric Device Defined from Materials Properties. *Energy Environ. Sci.* **2017**, *10*, 2280–2283. [[CrossRef](#)]
39. Kasap, S. *Thermoelectric Effects in Metals*; The Department of Electrical and Computer Engineering: Saskatoon, SK, Canada, 2001; pp. 1–11.
40. Shnawah, D.A.; Sabri, M.F.M.; Badruddin, I.A.; Said, S.B.M.; Ariga, T.; Che, F.X. Effect of Ag Content and the Minor Alloying Element Fe on the Mechanical Properties and Microstructural Stability of Sn-Ag-Cu Solder Alloy under High-Temperature Annealing. *J. Electron. Mater.* **2013**, *42*, 470–484. [[CrossRef](#)]
41. Liou, B.H.; Chen, C.M.; Horng, R.H.; Chiang, Y.C.; Wu, D.S. Improvement of Thermal Management of High-Power GaN-Based Light-Emitting Diodes. *Microelectron. Reliab.* **2012**, *52*, 861–865. [[CrossRef](#)]
42. Corning, D. SYLGARDTM 184 Silicone Elastomer Kit. Available online: <https://www.dow.com/en-us/pdp.sylgard-184-silicone-elastomer-kit.01064291z.html> (accessed on 30 July 2021).
43. Wang, Y.; Shi, Y.; Mei, D.; Chen, Z. Wearable Thermoelectric Generator for Harvesting Heat on the Curved Human Wrist. *Appl. Energy* **2017**, *205*, 710–719. [[CrossRef](#)]
44. ANSYS Inc. *ANSYS Workbench Product Release Notes 10.0*; ANSYS Inc.: Canonsburg, PA, USA, 2005.
45. Chen, Z.; Lin, M.Y.; Xu, G.D.; Chen, S.; Zhang, J.H.; Wang, M.M. Hydrothermal Synthesized Nanostructure Bi-Sb-Te Thermoelectric Materials. *J. Alloys Compd.* **2014**, *588*, 384–387. [[CrossRef](#)]
46. Mackey, J.; Dynys, F.; Sehirlioglu, A. Uncertainty Analysis for Common Seebeck and Electrical Resistivity Measurement Systems. *Rev. Sci. Instrum.* **2014**, *85*, 6. [[CrossRef](#)] [[PubMed](#)]
47. Mackey, J.; Dynys, F.; Sehirlioglu, A. *Uncertainty Analysis of Seebeck Coefficient and Electrical Resistivity Characterization*; NASA: Akron, OH, USA, 2013; Volume 24.
48. *Mechanical APDL Modeling and Meshing Guide*; ANSYS Inc.: Canonsburg, PA, USA, 2010; Volume 3304, pp. 724–746.
49. *ANSYS Mechanical APDL Modeling and Meshing Guide*; ANSYS 2020 R1 Release; ANSYS Inc.: Canonsburg, PA, USA, 2020.
50. European Thermodynamics Limited. Thermoelectric Generator Module GM250-449-10-12. Available online: <https://media.digikey.com/pdf/DataSheets/EuropeanThermodynamicsPDFs/GM250-449-10-12.pdf> (accessed on 3 October 2021).
51. Xiao, H.; Gou, X.; Yang, S. Detailed Modeling and Irreversible Transfer Process Analysis of a Multi-Element Thermoelectric Generator System. *J. Electron. Mater.* **2011**, *40*, 1195–1201. [[CrossRef](#)]